ACS ES&T Water

pubs.acs.org/estwater

Article

Mechanistic Insight into the Synergistic Removal of Metallic and Nonmetallic Cocontaminants in Water by Iron Nanoparticles

Ziwei Han and Adeyemi S. Adeleye*

Cite This: *ACS EST Water* 2024, 4, 3099−3109

Read Online

ACCESS | Metrics & More | Article Recommendations | Supporting Information

ABSTRACT: Industrial wastewaters with high concentrations of multiple classes of contaminants are challenging to treat and may require multistage treatment processes. This study aimed to develop and optimize a simple framework to simultaneously remove metals and nonmetals that commonly coexist in industrial wastewater. Based on a hypothesis that zerovalent iron (Fe^0) will synergistically remove metals (with a more positive standard reduction potential than Fe^{2+}/Fe^0; $E° = -0.44$ V) and anions via interconnected chemical processes, we studied the simultaneous removal of copper (Cu^{2+}) and phosphorus (P) using pristine and sulfidized nanoscale zerovalent iron (NZVI and SNZVI, respectively). The removal capacity of NZVI increased from 0.303 mg-Cu/m^2 and 1.650 mg-P/m^2 in single-contaminant systems to 1.136 mg-Cu/m^2 and 1.673 mg-P/m^2 in multicontaminant systems. We established that Fe^{2+}, a major product of Fe^0 and Cu^{2+} reactions, is a reactant in P precipitation that creates feedback. Sulfidation of NZVI (S/Fe = 0.28) enhanced the removal capacities to 3.140 mg-Cu/m^2 and 3.295 mg-P/m^2 in single-contaminant systems and 4.831 mg-Cu/m^2 and 4.803 mg-P/m^2 in multicontaminant systems because additional Fe^{2+} was produced by reactions between Cu^{2+} and FeS. Finally, we introduced a framework for using artificial neural networks (ANNs) to optimize the system.

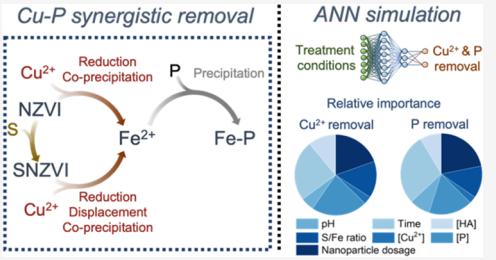

KEYWORDS: *heavy metals, nanotechnology, phosphate, industrial wastewater, artificial neural network (ANN), machine learning, water treatment*

1. INTRODUCTION

Heavy metals have profound adverse effects on humans and the ecosystem,[1,2] which necessitates decreasing human and environmental exposure. They are common in wastewater from industrial activities,[3−7] which needs to be treated to decrease metal concentration. The occurrence of nonmetallic cocontaminants often complicates the treatment of heavy metals as most existing water treatment techniques that are effective for removing metal ions (including chemical precipitation, electrochemical methods, and adsorption)[8,9] may not be as (cost) effective for the coexisting nonmetals.[10,11] For instance, phosphorus (P) often occurs with copper (Cu) in agricultural runoff or metal coating wastewater due to using P to increase the corrosion resistance of Cu tubing.[12] Chemical precipitation, e.g., with the use of sulfide (S^{2-}), can precipitate out copper sulfide (CuS; $K_{sp} = 7.9 \times 10^{-37}$) at extremely low concentrations of Cu^{2+} at which copper phosphate ($Cu_3(PO_4)_2$; $K_{sp} = 1.4 \times 10^{-37}$) cannot form.[13−15] While electrochemical methods effectively remove Cu^{2+} and P, widespread adoption is limited by their high operational cost.[16] Adsorption, using carbon materials, is a promising, low-cost technique. Still, competition among cocontaminants negatively impacts efficiency.[10,17] Therefore, simple treatment strategies that effectively and simultaneously remove cocontaminants (particularly metals and nonmetals) are needed.

This study is based on the central hypothesis that zerovalent iron, Fe(0), will synergistically remove metals with a more positive standard reduction potential than Fe^{2+}/Fe^0 ($E° = -0.44$ V) and nonmetals (such as P) via multiple interconnected chemical processes. The rationale for this hypothesis is that the dissolved Fe, produced during the oxidation of Fe(0),[18] can precipitate the anionic nonmetal in solution. To test the hypothesis, we selected Cu ($E° = 0.159$ V for Cu^{2+}/Cu^{1+} and 0.3419 V for Cu^{2+}/Cu^0) as the metallic contaminant and P as the nonmetallic cocontaminant since they are frequently detected in industrial wastewater.[12] Several existing studies have shown the efficacy of nanoscale zerovalent iron (NZVI) for individual metallic and nonmetallic contaminants,[19−21] but the novelty of this work is synergistically targeting multicontaminant systems. A study published earlier this year showed that NZVI can effectively remove both cadmium or nickel and P from water.[22] The authors attributed the enhanced performance of NZVI when both the metallic and nonmetallic contaminants were present to electrostatic

Received: May 11, 2024
Revised: June 7, 2024
Accepted: June 18, 2024
Published: July 2, 2024

interactions and specific binding sites.[22] However, we suspect that it may have more to do with synergies in pathways for removing both types of contaminants, which still need to be explored.

Additionally, incorporating sulfide species into NZVI to produce sulfidized NZVI (or SNZVI) improves chemical stability, reactivity, and biocompatibility.[23−26] However, it is unclear if sulfidation has any influence on the efficiency of NZVI in a multicontaminant system. Therefore, we investigated the performance of NZVI and SNZVI for the simultaneous removal of Cu^{2+} and P using experimental and analytical approaches. We also introduced a framework for using artificial neural networks (ANNs) to optimize the treatment, primarily by identifying the relative contributions of each variable in the cocontaminant treatment system. Unlike traditional simulation strategies, ANN does not require complex mathematical models and physical/chemical theorems.[27]

2. MATERIALS AND METHODS

2.1. Nanoparticle Synthesis and Characterization. Both pristine and sulfidated NZVI nanoparticles were synthesized under a nitrogen atmosphere based on published methods.[23] Briefly, to synthesize NZVI, 300 mL of 3 M sodium borohydride ($NaBH_4$; Acros Organics, Morris Plains, NJ) was titrated into 300 mL of 0.5 M ferric chloride ($FeCl_3$; Alfa Aesar, Ward Hill, MA) at a flow rate of 10 mL/min and a mixing speed of 600 rpm. For SNZVI, the $NaBH_4$ solution was mixed with 30 mL of 0.70 M sodium dithionite ($Na_2S_2O_4$; Millipore Sigma, Burlington, MA) before titrating into the $FeCl_3$ solution to achieve a theoretical sulfur/iron (S/Fe) molar ratio of 0.28 (denoted as $SNZVI_{0.28}$). To further investigate the role of sulfidation in the coremoval of Cu^{2+} and P, additional SNZVI nanoparticles with theoretical S/Fe molar ratios of 0.07, 0.14, and 0.21 (denoted $SNZVI_{0.07}$, $SNZVI_{0.14}$, $SNZVI_{0.21}$, respectively) were synthesized. The nanoparticles were separated from the aqueous phase using a magnetic field, washed with deoxygenated deionized (DI) water (18.2 MΩ·cm), dried in a vacuum oven at 60 °C (Napco 5831, Scotia, NY), and stored in a desiccator under a vacuum until use.

We determined the actual S/Fe molar ratio of the different SNZVI nanoparticles by analyzing the digested nanoparticles with an iCAP RQ-C2 inductively coupled plasma mass spectrometer (ICP-MS; Thermo Scientific, Waltham, MA). An FEI Magellan 400 scanning electron microscope (SEM; Hillsboro, OR) and a JEOL JEM-2800 transmission electron microscope (TEM; Japan) were used to characterize the morphology and size of the nanoparticles. We determined the nanoparticles' crystal structures with an Ultima-III X-ray diffractometer (XRD; Rigaku, Japan). The Brunauer−Emmett−Teller (BET) surface area of particles was determined by using a Micromeritics 3Flex (Norcross, GA). Based on established methods, we also determined their hydrodynamic sizes and zeta (ζ) potential using a Nanobrook 90Plus (Brookhaven Instruments, Holtsvile, NY).[28,29] Additional nanoparticle characterization details are provided in the Supporting Information (SI) Section S1.

2.2. Cu^{2+} and P Removal Using Iron Nanoparticles. We performed batch studies to determine the efficiency of the nanoparticles for removing Cu^{2+} and P in single- and multicontaminant systems. For the batch studies, we added known amounts of the stock solutions of the contaminant(s)—copper chloride ($CuCl_2$; Alfa Aesar) and/or potassium dihydrogen phosphate (KH_2PO_4; Fisher Scientific, Waltham, MA)—to DI water to achieve 100 mg/L each. The tested concentration was based on residual Cu and P concentrations in wastewater from coating operations (ten to hundreds of mg/L).[12,30] The solution was adjusted to pH 5 (using dilute HCl and NaOH) to prevent the precipitation of Cu^{2+} and P. A known volume of each nanoparticle stock suspension was then introduced into the contaminant solution to achieve 0.5 g/L nanoparticles. Each sample was mixed at 150 rpm and 20 °C for 2.5 h (using a Fisher Scientific Versa-Bath S Model 224) to promote contact between particles and dissolved contaminants. Additional experiments were performed to determine the role of nanoparticle dosage (0.1−0.5 g/L), nanoparticle S/Fe molar ratio (0−0.28), initial Cu^{2+} and P concentrations (0−100 mg/L), pH (3−11), and natural organic matter (NOM) concentration, which was represented by humic acid (HA; 0−20 mg/L), and treatment time (0−150 min). At the end of the batch experiments, we separated the solids via centrifugation at 18,000 *g* for 15 min (Southwest Science SC1024R, Hamilton Township, NJ). We validated this approach using filtration combined with ICP-MS (described in Section S2 and reported in Figure S1). We quantified the equilibrium concentrations of Cu^{2+} with the ICP-MS, while that of P was determined using the acid−molybdate method.[31] The data obtained from the batch studies were fitted to the classical adsorption isotherm and kinetic models, as described in Sections S3 and S4.

2.3. Spectroscopic Analyses of Obtained Solids. We investigated the reaction mechanism of the Fe−Cu−P system via X-ray analysis of the solids obtained from the batch studies using XRD. We also conducted X-ray photoelectron spectroscopic (XPS; Kratos AXIS Supra Shimadzu, Japan) analyses on the samples. While XRD probes materials up to a few microns, XPS provides quantitative surficial (~8 nm) material information.[32] XRD analysis was performed at beam angles between 20 and 90°. We scanned each sample for XPS analysis at a binding energy of −5 to 1400 eV (1.0 eV interval) with a 0.10 mA emission current. We then conducted a high-resolution analysis of the C 1s, P 2p, Cu 2p, Fe 2p, and S 2p regions (at 0.1 eV intervals and with an emission current of 20 mA) to obtain the binding information. The C 1s signal for adventitious carbon was used to calibrate the XPS data. We used the data obtained from XPS analysis to estimate the ratio of Cu^{2+} and P immobilized on the surface of the particles at equilibrium, as explained in Section S5. In addition to XRD and XPS, we collected the Raman spectra of the materials obtained after contaminant treatment using a Renishaw inVia Qontor Raman Microscope (Wotton, U.K.). Samples were analyzed using a Renishaw HPNIR785 instrument at a laser wavelength of 532 nm (1% laser power and 5 s exposure time).

2.4. Application of ANN to Experimental Data. To evaluate a framework for using machine learning to optimize nanotechnology-based water treatment, we developed an ANN function using MATLAB_R2018b. For the function, we considered seven features—nanoparticle dosage, nanoparticle S/Fe molar ratio, initial Cu^{2+} and P concentrations, pH, HA concentration, and treatment time—as input parameters. The Cu^{2+} and P removal efficiencies were the outputs. To increase the robustness of the function, we collected suitable data from the literature in addition to the experimental data obtained from this study for ANN training and testing. Most of the data we found were obtained from investigations of the efficacy of NZVI for Cu^{2+} or P removal, except one data set on using

https://doi.org/10.1021/acsestwater.4c00441
ACS EST Water 2024, 4, 3099−3109

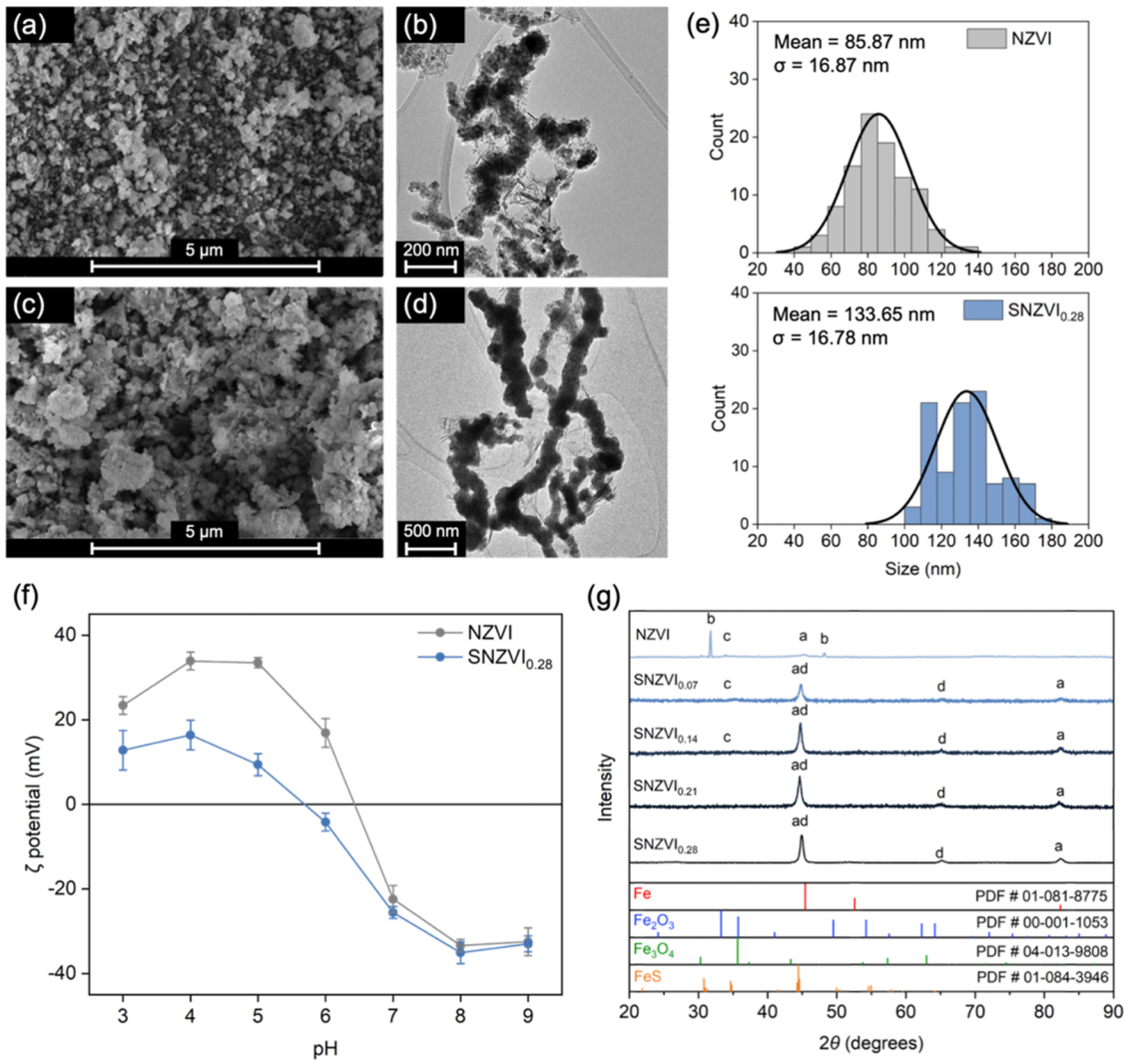

Figure 1. (a) SEM and (b) TEM micrographs of NZVI; (c) SEM and (d) TEM micrographs of $SNZVI_{0.28}$. (e) Size distributions of NZVI and $SNZVI_{0.28}$. The mean particle sizes were calculated by measuring 100 particles. (f) ζ-potential of NZVI and $SNZVI_{0.28}$ at different pH values (adjusted using dilute NaOH and HCl). (g) X-ray diffractograms of freshly prepared NZVI and SNZVI with different S/Fe ratios (a = Fe; b = Fe_2O_3; c = Fe_3O_4; and d = FeS).

SNZVI for Cu^{2+} removal.[33−37] All of the input and output values were normalized using the min−max method eq 1.[38]

$$x_i = 2 \times \frac{x_i - x_{\min}}{x_{\max} - x_{\min}} - 1 \quad (1)$$

where x_i is the experimental data and $x_{\min}$ and $x_{\max}$ are the minimum and maximum values of the parameter x_i, respectively.

For the ANN setup, 80 and 20% of the experimental data were used for training and testing, respectively. The Bayesian regularization algorithm with two hidden layers, containing eight and three neurons in the first and second hidden layers, respectively, was used for initial function configurations. The generated ANN function was accepted when the correlation coefficients between the simulated and experimental Cu^{2+} and P removal efficiency in training, testing, and their combination were greater than 0.95. The accuracy of the ANN function was assessed by calculating the root mean square error (RMSE). The relative importance and sensitivity of each of the seven input parameters were determined using Garson's algorithm eq 2 and the partial derivative algorithm eq 3, respectively[27,39]

$$I_j = \frac{\sum_{m=1}^{N_h} [(|W_{jm}^{ih}| / \sum_{k=1}^{N_i} |W_{km}^{ih}|) \times |W_{mn}^{ho}|]}{\sum_{k=1}^{N_i} \{\sum_{m=1}^{N_h} [(|W_{km}^{ih}| / \sum_{k=1}^{N_i} |W_{km}^{ih}|) \times |W_{mn}^{ho}|]\}} \quad (2)$$

$$S = W^{ho} \times f'_{h2} \times W^{h2h1} \times f'_{h1} \times W^{ih} \quad (3)$$

$$f_{h1} = f_{h2} = \frac{2}{1 + e^{-2x}} - 1 \quad (4)$$

where I_j is the relative importance of the jth input parameter and W is the connection weight matrix obtained from the ANN function. The superscripts (i, h, and o) on W indicate the input, hidden, and output layers, respectively, while the subscripts (k, m, and n) denote the input, hidden, and output neurons, respectively. N_i and N_h are the numbers of inputs and neurons, respectively. S is the sensitivity matrix; f_{h1} and f_{h2} are the activation functions in the first and second hidden layers of neurons (described in eq 4); and x is the input matrix to hidden layer neurons.

2.5. Data and Statistical Analysis. We assessed all of the data sets for normality and homogeneity of variance using the Shapiro−Wilk and Levene tests, respectively, for which

https://doi.org/10.1021/acsestwater.4c00441
ACS EST Water 2024, 4, 3099−3109

acceptance was based on $p > 0.05$. Statistical significance of differences among treatment groups was determined using either ANOVA, followed by two-sample Tukey's tests for parametric data sets, or Kruskal–Wallis test by ranks for nonparametric data sets. The statistical analyses were conducted using SPSS Statistics software (version 25.0).

3. RESULTS AND DISCUSSION

3.1. Characterization of Iron Nanoparticles. Sulfidation of NZVI to create $SNZVI_{0.28}$ led to increased primary particle size and surface roughness (Figure 1a–d). The mean particle size of NZVI was 85.9 ± 16.9 nm, while that of $SNZVI_{0.28}$ was 133.7 ± 16.8 nm (Figure 1e). The BET surface area of $SNZVI_{0.28}$ (41.5 m^2/g) was smaller than that of NZVI (95.2 m^2/g), which agrees with what we expected based on their primary particle sizes. The hydrodynamic diameters of NZVI (280.6 ± 9.2 nm) and $SNZVI_{0.28}$ (286.5 ± 2.8 nm) were statistically similar at pH 7 ($p = 0.431$, Figure S2). In the same vein, there was no statistical difference ($p = 0.265$) between the ζ-potential of NZVI (−22.4 ± 3.2 mV) and $SNZVI_{0.28}$ (−25.6 ± 1.4 mV) at pH 7. However, we found that $SNZVI_{0.28}$ (pH_{IEP} = 5.7) has a lower isoelectric point than NZVI (pH_{IEP} = 6.4), as shown in Figure 1f.

We confirmed the incorporation of S into the SNZVI nanoparticles by ICP-MS analysis using ^{34}S (instead of the abundant ^{32}S) to avoid interference from the oxygen dimer ($^{16}O^{16}O^{+}$).[40] The measured S/Fe molar ratio of $SNZVI_{0.07}$, $SNZVI_{0.14}$, $SNZVI_{0.21}$, and $SNZVI_{0.28}$ was 0.03 ± 0.01, 0.13 ± 0.01, 0.19 ± 0.02, and 0.25 ± 0.03 (Table S1), respectively. The closeness of the theoretical and measured S/Fe molar ratios shows that the synthesis approach we used in this study is reliable. The X-ray diffractogram of NZVI revealed that the nanoparticle mainly consists of Fe(0) (2θ = 45.2° and 83°), Fe_2O_3 (2θ = 32° and 48°), and Fe_3O_4 (2θ = 31° and 35°),[24,41,42] indicating that the nanoparticles were partially oxidized (Figure 1g). The iron oxide peaks were weak at the lowest sulfidation amount ($SNZVI_{0.07}$) and undetected at higher sulfidation amounts, resulting in higher Fe(0) content in SNZVI than NZVI (Table S1). Incorporating S into NZVI was further confirmed by a weak FeS peak at 2θ = 66° and a Fe(0) peak shift from 45.2 to 44.8 − 45.0°, which were also reported by others.[43]

3.2. Removal of Individual and Combined Contaminants in Water. *3.2.1. Cu^{2+} Removal by Iron Nanoparticles.* The modeled maximum adsorption capacities are reported in Table S2, while the measured capacities after 150 min are reported in this section of the main manuscript. Sulfidation of NZVI affected Cu^{2+} removal efficiency, but the type and extent of effect were S/Fe molar-ratio-dependent. As the theoretical nanoparticle S/Fe ratio increased from 0 to 0.07 (at pH 5), the measured removal capacity for Cu^{2+} (in the absence of P) significantly ($p = 0.005$) decreased from 0.378 ± 0.057 mg-Cu/m^2 to 0.111 ± 0.035 mg-Cu/m^2 (Figure 2a). However, the Cu removal capacity increased as the theoretical nanoparticle S/Fe ratio increased above 0.07. The best performance was observed with $SNZVI_{0.28}$ (3.133 ± 0.183 mg-Cu/m^2), which is about an order of magnitude higher than we observed with NZVI. We adduce the initial adverse impact of sulfidation on Cu^{2+} removal to a combination of lower surface area (surface area decreased with sulfidation, Table S1) and negligible FeS_x content (FeS_x amount increased with increasing sulfidation). Interestingly, we observed a similar trend (an initial decrease followed by an increase in removal capacity) in a previous study, in which we used NZVI and SNZVI to remove cadmium from water.[44] Since $SNZVI_{0.28}$ performed better than the other S/Fe ratios we focused on $SNZVI_{0.28}$ for most of this study.

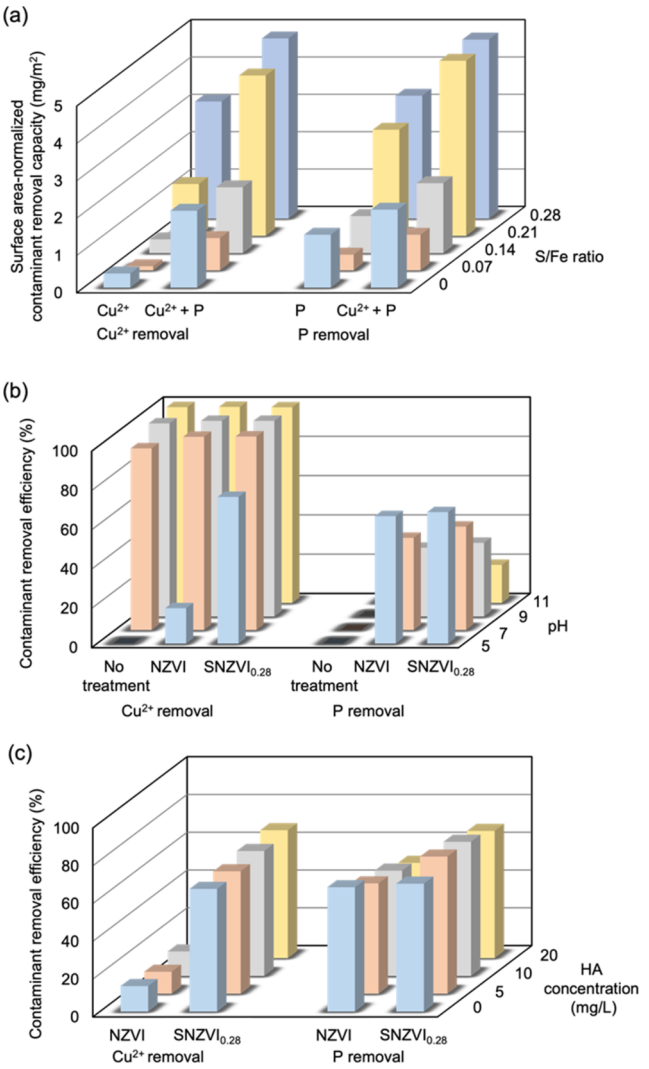

Figure 2. (a) Surface area-normalized Cu^{2+} and P removal capacities by NZVI and SNZVI. Cu^{2+} or P removal efficiencies of NZVI/SNZVI at different (b) pH and (c) humic acid (HA) concentrations. The initial [Cu^{2+}] = [P] = 100 mg/L; [NZVI] = [SNZVI] = 0.5 g/L; pH = 5 in panels (a, c). The S/Fe ratio represents the theoretical molar ratio.

In addition to high removal capacity, we also observed that the rate of Cu^{2+} removal increased when we used $SNZVI_{0.28}$ (pseudo-second-order rate constant [k_2] = 0.059 m^2/mg·min) compared to NZVI (k_2 = 0.038 m^2/mg·min), as shown in Table S2. In addition, the Cu^{2+} removal performance of the nanoparticles was not adversely affected by the water chemistry parameters expected in real wastewater (Section S5). In fact, Cu^{2+} removal increased as the solution pH increased above 5 (Figure 2b), and NOM increased up to 20 mg/L (Figure 2c). Precipitation of Cu^{2+} (Figure S3) substantially contributed to high Cu^{2+} removal at neutral and alkaline pH, as evidenced by high Cu^{2+} removal in the absence of the nanoparticles (Figure 2b). However, adsorption may have also been enhanced by increased negativity of the nanoparticles (Figure 1f). We attribute the slight enhancement in Cu^{2+} removal in the

https://doi.org/10.1021/acsestwater.4c00441
ACS EST Water 2024, 4, 3099−3109

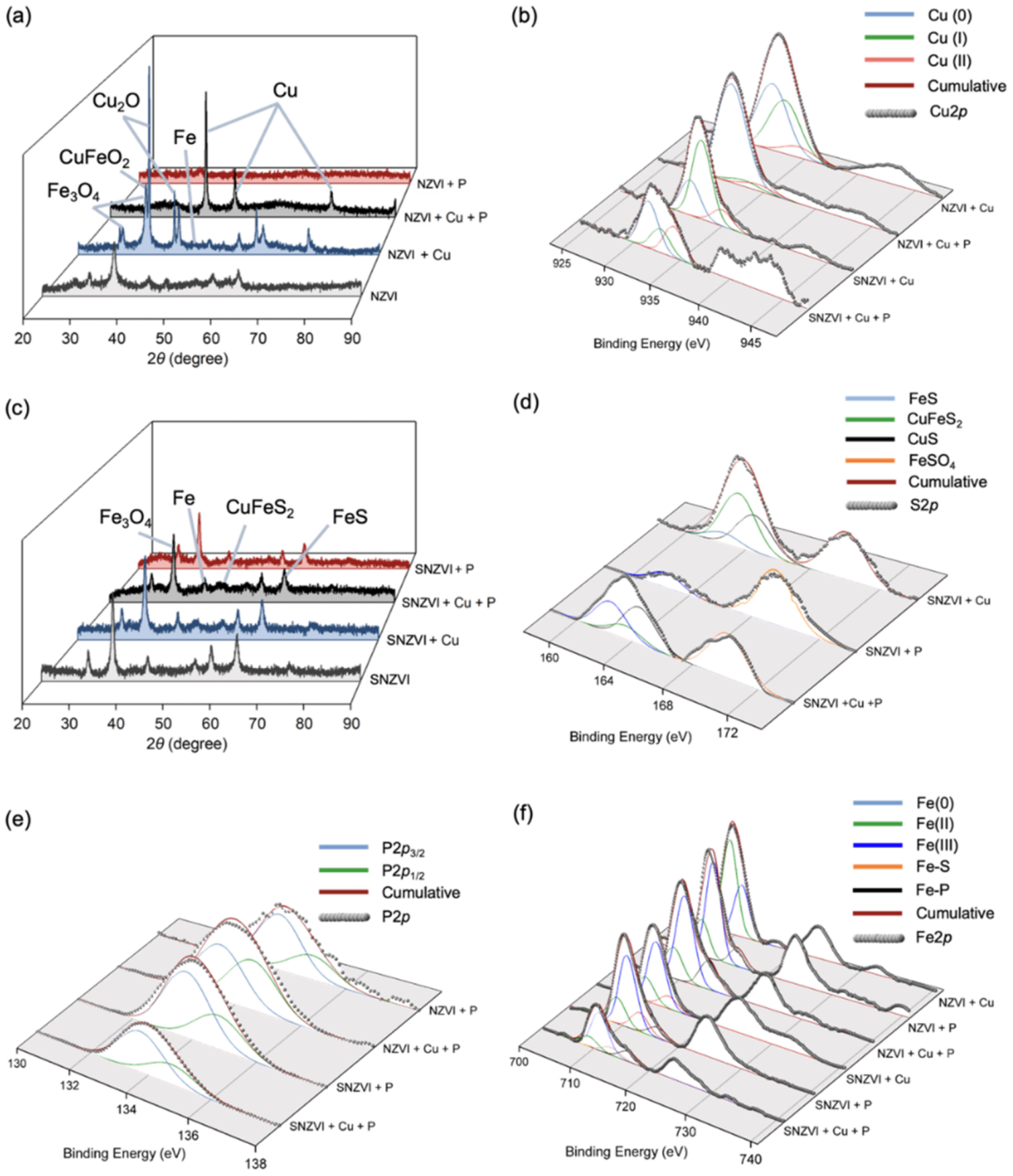

Figure 3. XRD diffractograms of (a) NZVI and (c) $SNZVI_{0.28}$ after treatment, and high-resolution (b) Cu 2p, (d) S 2p, (e) P 2p, and (f) Fe 2p XPS spectra of NZVI/$SNZVI_{0.28}$ obtained from the Cu/P individual or cocontaminant system. (Initial $[Cu^{2+}]$ = [P] = 100 mg/L; initial [NZVI] = $[SNZVI_{0.28}]$ = 0.5 g/L; treatment time = 150 min; pH = 5). Traditional versions of the diffractograms (a, b) with all of the characteristic labels are provided in Figure S5a,b.

presence of HA to additional adsorption of the metallic ions (e.g., via electrostatic interaction and complexation) by HA bound to the surface of nanoparticles.[45]

XRD analysis of the solids obtained after the batch reaction revealed Cu(0) (2θ = 43, 51, and 74°) and Cu_2O peaks (2θ = 42 and 62°), a strong Fe_3O_4 peak (2θ = 31 and 35°), and a weak Fe(0) peak in the NZVI system (Figures 3a, S4a, and S5a). These peaks indicate the thermodynamically favorable reduction of Cu^{2+} to Cu(0) and Cu(I) and the oxidation of Fe(0) to Fe(II), according to eqs 5 and 6. Dissolved Fe concentration (measured after 2.5 h using the ICP-MS) increased significantly (p = 0.049) from 2.1 ± 0.5 mg/L without Cu^{2+} in NZVI suspension to 8.6 ± 3.3 mg/L when Cu^{2+} was present (Figure S7), confirming the production of Fe^{2+}. The peak ratio of Cu(0) to Cu_2O increased over time (Figure S4a), suggesting the sequential reduction of Cu^{2+}. In addition to Cu(0) and Cu_2O, XRD also revealed the presence of $CuFeO_2$ (2θ = 36°), which was formed from the precipitation of Cu^{2+} and Fe^{2+} in water eq 7. The reduction of Cu^{2+} by NZVI was corroborated by XPS analysis (Figure 3b). The scan of the Cu 2p peak revealed that the Cu species on the surface of the solids obtained from the NZVI system primarily consisted of Cu(0) (binding energy [BE] = 932.8 eV; 53.6 at. %), Cu(I) (BE = 934 eV; 40.8 atom %), and Cu(II) (BE = 935.4 eV; 5.6 atom %).[46] In summary, NZVI removed

https://doi.org/10.1021/acsestwater.4c00441
ACS EST Water 2024, 4, 3099−3109

Cu^{2+} from the aqueous phase in the absence of P via reduction, precipitation, and adsorption.

We observed some distinct Cu^{2+} removal mechanisms in the SNZVI system with NZVI. For instance, in addition to the peaks for Cu(0) and Cu(I), formed from the reduction of Cu^{2+}, we also observed $CuFeS_2$ (2θ = 29 and 46°) in the solids when SNZVI was used for treatment (Figures 3c, S5b, and S7a). $CuFeS_2$ (K_{sp} = 3.33 × 10^{-66}) was formed from the precipitation of Cu^+ and the FeS in SNZVI eq 8. The reaction quotient (Q = 1.96) of this reaction eq 8 that we calculated based on the concentrations of all of the species present at the end of the treatment was lower than the equilibrium constant (K = 6.41 × 10^{14}), indicating limited reactants (likely FeS) in the system. The Raman spectra that we obtained indicated the existence of Cu−S (Raman shift = 269 cm^{-1}) and S−S (Raman shift = 474 cm^{-1}) bonds in the reacted particles (Figure S6b). XPS also confirmed the presence of $CuFeS_2$ at BE = 163.5 eV (Figure 3d). In addition to $CuFeS_2$, XPS also revealed the formation of CuS (BE = 164.5 eV)—a product of a displacement reaction in the presence of excess Cu^{2+}—in the SNZVI system eq 9.[35]

Upon deconvoluting the Cu 2p XPS peak, we found that Cu(I) (61.7 atom %), derived from $CuFeS_2$ and Cu_2O, was the dominant form of Cu on the surface of the solid phase, followed by Cu(0) (27.9 atom %), and then Cu(II) (12.8 atom %) (Figure 3b). Like the NZVI system, the dissolved Fe concentration increased in the SNZVI system during Cu^{2+} removal (Figure S7a). In this case, we detected only 0.1 ± 0.0 mg/L dissolved Fe after 2.5 h without Cu^{2+} (due to the high stability of SNZVI), but the dissolved Fe increased to 62.9 ± 1.8 mg/L when Cu^{2+} was present. The large increase in dissolved Fe concentration (compared to the NZVI system) resulted from the additional reactions with FeS in the SNZVI system eqs 8 and 9. Therefore, in addition to the Cu^{2+} immobilization mechanisms observed with NZVI, SNZVI also immobilized Cu^{2+} via coprecipitation with FeS (resulting in $CuFeS_2$ formation) and displacement of FeS (to produce CuS), both of which are thermodynamically favorable reactions eqs 8 and 9.

$$Cu^{2+} + Fe + Cu + Fe^{2+} \quad \Delta G = -150.5\ kJ/mol \tag{5}$$

$$2Cu^{2+} + Fe + H_2O \rightarrow Cu_2O + Fe^{2+} + 2H^+ \quad \Delta G = -129.8\ kJ/mol \tag{6}$$

$$Cu^{2+} + Fe^{2+} + 2H_2O \rightarrow CuFeO_2 + 4H^+ \quad \Delta G = -82.11\ kJ/mol \tag{7}$$

$$Cu^{2+} + 2FeS \rightarrow CuFeS_2 + Fe^{2+} \quad \Delta G = -84.47\ kJ/mol \tag{8}$$

$$Cu^{2+} + FeS \rightarrow CuS + Fe^{2+} \quad \Delta G = -97.53\ kJ/mol \tag{9}$$

3.2.2. P Removal by Iron Nanoparticles. Similar to what we observed with Cu^{2+} removal, sulfidation of NZVI initially inhibited P removal and then improved it (both in terms of performance and kinetics) with increasing S/Fe ratio (Figure 2a). As an example, the measured removal capacity of $SNZVI_{0.07}$ for P (0.421 ± 0.032 mg-P/m^2) was significantly (p < 0.001) lower than that of NZVI (1.418 ± 0.007 mg-P/m^2) after 150 min treatment. Meanwhile, when the S/Fe ratio reached 0.28 (that is, $SNZVI_{0.28}$), P removal was 3.287 ± 0.035 mg-P/m^2, which was more than twice as high as the capacity of NZVI for P. The XRD diffractograms of the solids obtained from the NZVI system after treating P had broad, weak intensities, suggesting that the nanoparticles became amorphous during treatment (Figures 3a,c, S4b,c, and S8b,c). We, however, observed a $-PO_4$ peak (BE = 134 eV) in the XPS spectra obtained from the NZVI system (Figure 3e) and a Fe−P bond (Raman shift = 1003 cm^{-1}) in the Raman spectra (Figure S6a), which suggests P adsorption to the nanoparticles. In addition, we identified a Fe(II)−P bond (BE = 717 eV) when the Fe 2p peak was deconvoluted (Figure 3f), which indicates binding between Fe(II) and P (according to eqs 10−11).[46,47] In contrast, the solids obtained from the SNZVI systems were crystalline, based on XRD analysis, further supporting the notion that sulfidation improves the chemical stability of NZVI. Furthermore, this was based on the deconvolution of the high-resolution XPS spectra (Figure 3e,3f) and Raman spectra (Figure S6b), we confirmed that SNZVI immobilized P in a similar way to NZVI, which was by chemisorption via coprecipitation/complexation (of $Fe_3(PO_4)_2$, $FeHPO_4$, or $Fe(H_2PO_4)_2$) with dissolved Fe eq 12.

To confirm the role of Fe^{2+} vs Fe particles in P removal eqs 11−12, we introduced an excess of a Fe^{2+} chelating ligand, 1,10-phenanthroline eq 13, to the nanoparticle suspensions before adding P. We found that P removal by NZVI and $SNZVI_{0.28}$ decreased from 67.0 ± 0.5% and 68.1 ± 1.0% (without phenanthroline), respectively, to 13.2 ± 0.2% and 5.3 ± 0.4% (with phenanthroline), respectively (Figure S7c). This shows that the nanoparticles and, much more so, their dissolved Fe played substantial roles in P removal. Therefore, it was unsurprising that P removal by NZVI and SNZVI decreased at high pH and in the presence of NOM (Figure 2b,c) since both conditions lead to decreased Fe^{2+}.[37,42,48,49] We admit that other factors, such as the increase in negative nanoparticle surface charge due to pH and NOM, competition with OH^- and NOM molecules (Section S5 and Figures 1f, S3, S9, and S10), etc., could also contribute to the decreased P removal we observed at pH > 5 and in the presence of NOM.

$$2Fe + 2H_2O + O_2 \rightarrow 2Fe^{2+} + 4OH^- \quad \Delta G = -334.6\ kJ/mol \tag{10}$$

$$Fe^{2+} + H_yPO_4^{y-3} \rightarrow Fe_{3-y}(H_yPO_4)_2 (y = 0, 1, \text{or } 2) \tag{11}$$

$$X + H_yPO_4^{y-3} \rightarrow X{\cdot}H_yPO_4^{y-3} \quad (X \text{ denotes active Fe sites on nanoparticles}) \tag{12}$$

$$Fe^{2+} + 3\ \text{phenanthroline} \rightarrow Fe(\text{phenanthroline})_3^{2+} \tag{13}$$

3.2.3. Cu^{2+} and P Coremoval by Iron Nanoparticles. To test the hypothesis that when Cu^{2+} and P coexist, their respective reactions with Fe(0) could synergistically enhance the removal of both contaminants, we conducted additional batch experiments in which the initial concentrations of Cu^{2+} and P were kept at 100 mg/L (as in the individual contaminant studies). ICP-MS analysis of the liquid phase after adsorption studies revealed that the coexistence of Cu^{2+} and P in the treatment system substantially increased the removal capacity

https://doi.org/10.1021/acsestwater.4c00441
ACS EST Water 2024, 4, 3099−3109

Scheme 1. Summary of Cu^{2+} and P Removal Mechanisms by NZVI and SNZVI

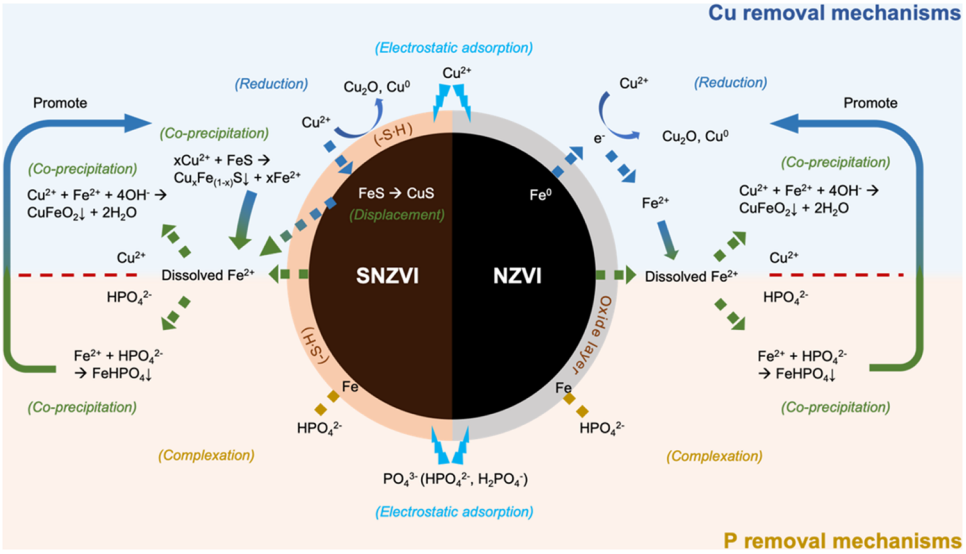

of the nanoparticles for Cu^{2+} by 1.5−7.8 fold and P by 1.5−2.6 fold (depending on the S/Fe molar ratio), relative to the single-contaminant systems (Figure 2a). At the end of 150 min of the adsorption study, the highest measured removal capacity for both Cu^{2+} and P was obtained with $SNZVI_{0.28}$ (4.819 ± 0.010 mg-Cu/m^2 and 4.790 ± 0.014 mg-P/m^2), and nearly 100% removal of both contaminants was achieved in the NZVI and $SNZVI_{0.28}$ systems. Surface analysis of the obtained solids via XPS corroborated the ICP-MS results based on the higher ratios of Cu/Fe and P/Fe in the solids obtained from the multicontaminant systems compared to each of the individual contaminant systems (Figure S11). For instance, the ratio of Cu 2p/Fe 2p peak areas increased from 0.18 in the NZVI-based single-contaminant system and 0.33 in the $SNZVI_{0.28}$-based single-contaminant system to 0.27 in the NZVI-based multicontaminant system and 0.35 in the $SNZVI_{0.28}$-based multicontaminant system.

To benchmark the efficacy of the nanoparticles in single- and multicontaminant systems, we compared their performance to that of a similar mass of granular-activated carbon (GAC), a widely used treatment media in the (waste)water industry. The amount of Cu^{2+} and P removed by the nanoparticles in both single- and cocontaminant systems was orders of magnitude higher than that removed by GAC, which achieved 0.032 ± 0.003 to 0.038 ± 0.005 mg-Cu/m^2 and 0.005 ± 0.001 to 0.010 ± 0.003 mg-P/m^2 at the same particle dose (0.5 g/L) and contaminant(s) concentration (100 mg/L). Compared to the single-contaminant treatment systems, the removal of Cu^{2+} and P decreased when they coexisted in the GAC treatment system due to competition (Figure S12), as expected from a primarily adsorption-based treatment system. This highlights the limitations of traditional adsorbents, such as GAC, for the treatment of water with multiple contaminants.

The decreased efficiency of the GAC treatment system in the presence of multiple contaminants shows the advantage of a treatment system with multiple mechanisms. It also demonstrates the practicality of using iron nanoparticles for waste streams of an appropriate metal and nonmetal. In the Cu−P multicontaminant system studied here, the Fe^{2+} produced from Cu^{2+} reduction eqs 5, 6, and 8 and displacement eq 9 serves as a reactant for the precipitation of P eq 11. The consumption of produced Fe^{2+} when P is present eq 11 causes reaction quotients of the Cu^{2+}-consuming reactions eqs 5, 6, 8, and 9 to be less than their respective equilibrium constants ($q < k$). According to Le-Chatelier's principle, when $q < k$, reactions shift to the right. This implies more Cu^{2+} reduction and displacement and, therefore, formation of more Fe^{2+} that will precipitate any remaining P. Hence, in theory, Fe^{2+} is always present as long as neither reactant is fully consumed. This synergy in the primary reactions for removing both contaminants leads to enhanced removal when both are present in water (Scheme 1).

The amount of dissolved Fe we found in the multicontaminant system decreased relative to when only Cu^{2+} was treated (Figure S7a). This further shows that Fe^{2+} plays a vital role in removing P in the multicontaminant system, like in the P-only system. Chelation of Fe^{2+} by 1,10-phenanthroline led to a significant ($p < 0.001$) decrease in P and Cu^{2+} removal (Figure S7b,c). For NZVI, the removal efficiencies significantly decreased from 98.2 ± 0.3% (for Cu^{2+}) and 99.0 ± 1.8% (for P) without phenanthroline to 59.1 ± 0.4% (for Cu^{2+}, $p < 0.001$) and 35.0 ± 1.0% (for P, $p < 0.001$) when phenanthroline was present. The decrease in performance was even more pronounced with SNZVI, with the removal of Cu^{2+} and P dropping below 6%. The higher impact of the chelating agent on the SNZVI treatment system is likely due to the complexation of phenanthroline onto FeS in SNZVI, which inhibited most of the FeS-based surface reactions.[50]

In addition to the noted higher removal of Cu^{2+} and P by the nanoparticles when both contaminants were present, the removal kinetics were also enhanced in the multicontaminant system (Table S2). For instance, k_2 increased from 0.038 m^2/mg Cu-min and 0.383 m^2/mg P-min in the NZVI-based single-contaminant systems to 0.628 m^2/mg Cu-min and 1.016 m^2/mg P-min. Meanwhile, k_2 increased from 0.059 m^2/mg Cu-min and 0.393 m^2/mg P-min in $SNZVI_{0.28}$-based single-contaminant systems to 1.189 m^2/mg Cu-min and 1.260 m^2/mg P-min. A substantial increase in reaction kinetics likely resulted from the Fe^{2+}-based feedback and enhanced Cu^{2+} and P diffusion described in the next paragraph.

https://doi.org/10.1021/acsestwater.4c00441
ACS EST Water 2024, 4, 3099−3109

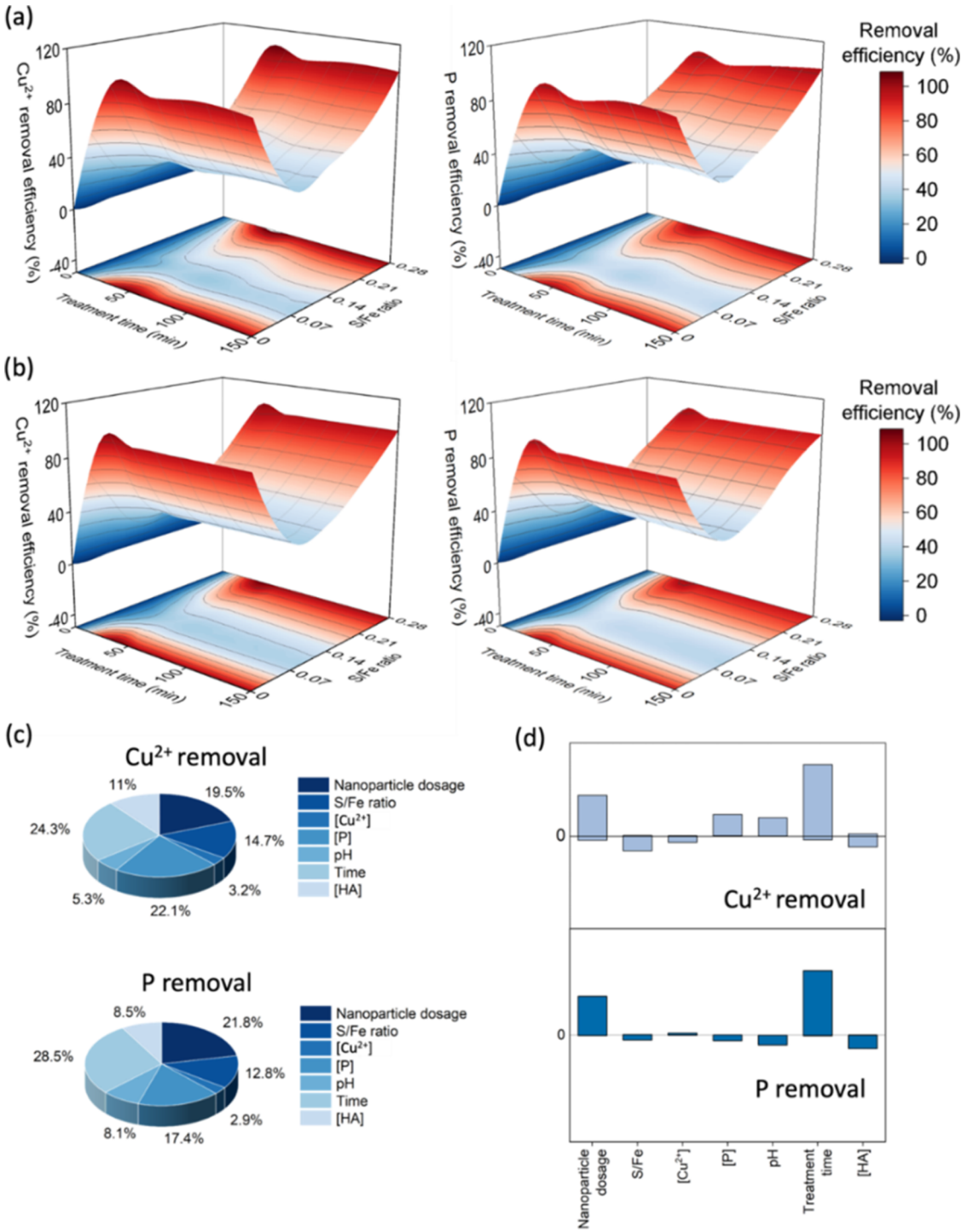

Figure 4. (a) Experimental and (b) simulated Cu^{2+} and P removal efficiencies with ANN, (c) relative importance, and (d) sensitivity analysis results of the ANN model.

Apart from leading to enhanced P precipitation, increased Fe^{2+} production likely encouraged fast corrosion of the nanoparticles, which must have improved the diffusion of the contaminants into the nanoparticles, further improving contaminant removal performance and kinetics.[33] To investigate the possibility of enhanced diffusion of Cu^{2+} and P into the nanoparticles during treatment, we compared the particle surface and bulk elemental composition using XPS and ICP-MS (see full details in Section S6 and Table S3). The fraction of removed Cu and P on the surface of NZVI (22 and 87%, respectively) in the cocontaminant system was lower than that in the single-contaminant systems (86 and 92%, respectively). We observed a similar trend in the $SNZVI_{0.28}$ system, in which the amount of Cu and P immobilized on the nanoparticle surface decreased from 16 and 61%, respectively, in the single-contaminant systems to 13 and 60%, when both were simultaneously present. These results support the hypothesis that the diffusion of Cu^{2+} and P into NZVI and $SNZVI_{0.28}$ was enhanced when both contaminants were present in the aqueous phase.

https://doi.org/10.1021/acsestwater.4c00441
ACS EST Water 2024, 4, 3099−3109

Since nearly all of the Cu^{2+} and P were removed by the nanoparticles when their initial concentrations were 100 mg/L, we challenged the particles with much higher amounts of the contaminants (1000 mg/L each) to access their application for highly polluted waters. We noticed only a small, insignificant (p = 0.061 for Cu^{2+} removal and p = 0.074 for P removal) increase in the removal capacities of NZVI, which increased from 2.059 ± 0.005 mg-Cu/m^2 and 2.088 ± 0.012 mg-P/m^2 when each contaminant was present at 100 mg/L to 2.532 ± 0.259 mg-Cu/m^2 and 2.465 ± 0.128 mg-P/m^2 when each contaminant was present at 1000 mg/L (Figure S13). These were close to the maximum removal capacity derived from the Langmuir isotherm model (2.626 mg-Cu/m^2 and 2.689 mg-P/m^2, Table S4). In contrast, the increases in the removal capacities of $SNZVI_{0.28}$ were large and significant (p = 0.002 for Cu^{2+} removal and p = 0.022 for P removal). The performance of SNZVI increased from 4.792 ± 0.183 mg-Cu/m^2 and 4.826 ± 0.039 mg-P/m^2 when each contaminant was present at 100 mg/L to 6.015 ± 0.219 mg-Cu/m^2 and 6.019 ± 0.458 mg-P/m^2 when each contaminant was present at 1000 mg/L. The Langmuir isotherm model suggested that the maximum removal capacities of $SNZVI_{0.28}$ could reach 9.277 mg-Cu/m^2 and 7.542 mg-P/m^2 (Table S4). These results demonstrate the advantage of sulfidation in the performance of iron nanoparticles.

3.3. Application of ANN to Experimental Data. The ANN architecture comprises two hidden layers with eight and three neurons in the first and second hidden layers, respectively (see the architecture in Figure S14a). The output parameters were the Cu^{2+} and P removal efficiencies. The selected transfer functions had a correlation coefficient of >0.97 between target and simulated output values in training, testing, and both (Figure S14b). The RMSE values for simulated Cu^{2+} and P removal were 2.2 and 5.8%, respectively. To confirm the ability of the ANN function to predict the experimental system accurately, we used it to predict Cu^{2+} and P removal efficiencies by varying the treatment time (0−150 min) and S/Fe ratio (0−0.28) while fixing the other input parameters (nanoparticle dosage = 0.5 g/L; initial [Cu^{2+}] and [P] = 100 mg/L; pH = 5; [HA] = 0 mg/L). As shown in Figure 4a,b, the simulation was consistent with the experimental data (RMSE = 3.2%), indicating high accuracy.

By applying Garson's eq eq 2 using the weight matrix obtained from the ANN function (Table S5), we determined the relative importance of each input parameter on Cu^{2+} and P removal by the iron nanoparticles. The trend of the relative importance of the input parameters to Cu^{2+} removal was treatment time (24.3%) > initial P concentration (22.1%) > nanoparticle dosage (19.5%) > S/Fe ratio (14.7%) > humic acid concentration (11%) > pH (5.3%) > initial Cu^{2+} concentration (3.2%), as shown in Figure 4c. For P removal, the trend was treatment time (28.5%) > nanoparticle dosage (21.8%) > initial P concentration (17.4%) > S/Fe ratio (12.8%) > humic acid concentration (8.5%) > pH (8.1%) > initial Cu^{2+} concentration (2.9%). Treatment time was the most important parameter, which agreed with the fast kinetics of removing Cu^{2+} and P when both were present. This also implies that increasing reaction time could significantly improve the treatment process owing to the synergy of the reactions. Nanoparticle dosage was substantially more influential than pH, suggesting that using NZVI/SNZVI would remove Cu^{2+} and P more effectively than adjusting pH. This also agrees with our experimental data, which shows that P removal is less sensitive to pH as Cu^{2+}. Interestingly, the initial P concentration was more essential in the multicontaminant treatment system than the initial Cu^{2+} concentration. This suggests that P may be the limiting reactant in the multicontaminant system. This is likely due to faster removal of P (k_2 = 1.016 m^2/mg-min using NZVI and 1.260 m^2/mg-min using $SNZVI_{0.28}$) than Cu^{2+} (k_2 = 0.628 m^2/mg-min using NZVI and 1.189 m^2/mg-min using $SNZVI_{0.28}$) in the multicontaminant system.

To assess the sensitivity and direction of impact (positive or negative) of each input parameter on Cu^{2+} and P removal efficiencies in multicontaminant systems, we used the partial derivative algorithm eq 3 to calculate the range of slope of each variable at 1000 sets of randomly generated inputs (within the range of the experimental conditions). As shown in Figure 4d, the nanoparticle dosage, initial P concentration, pH, and treatment time positively impacted the Cu^{2+} removal system. In contrast, the initial Cu^{2+} concentration mainly had an adverse effect on the Cu^{2+} removal efficiency. Depending on their actual values, the S/Fe ratio and humic acid concentration could positively or negatively impact the Cu^{2+} removal efficiency. The P removal efficiency decreased with an increase in initial P concentration or pH for the P treatment system. The negative impact of pH was likely due to electrorepulsive effects between the nanoparticles and phosphate anions as pH increases. Nanoparticle dosage and initial Cu^{2+} concentration positively impacted P removal, while the rest of the treatment conditions could have positive or negative effects depending on their values. Treatment time had the highest absolute sensitivity for both Cu^{2+} and P removal, which is related to the fast removal rates.

4. CONCLUSIONS AND IMPLICATIONS

Our investigation of the simultaneous removal of Cu^{2+} and P using NZVI and SNZVI revealed that Fe^{2+}, the main byproduct of the redox and displacement reactions between Cu^{2+} and Fe-based nanoparticles, serves as a reactant for the precipitation of P. The consumption of Fe^{2+} by P drives Cu^{2+} removal, which feeds back into P removal, causing more and faster removal of both contaminants from water (in comparison to when only one of both contaminants was present or a traditional adsorption treatment system). The principle behind the synergistic treatment process described in this study is expected to apply broadly to wastewaters with metallic and nonmetallic constituents, as long as the metal has an $E°$ > −0.44 V (such as cobalt ($E°$ = −0.28 V), nickel ($E°$ = −0.26 V), and lead ($E°$ = 0.95 V)) and the nonmetal can precipitate with Fe (like sulfide, silicate, and carbonate). Waste streams that would typically have these types of constituents include metal-plating wastewater, agricultural runoff, mining and smelting wastewater, and battery and textile manufacturing wastewater.

One of the goals of waste treatment is cost-effectiveness. Although increasing the amount of the primary treatment agent (e.g., nanoparticle dose in this study) is often considered a way to improve performance, the application of machine learning to model the treatment systems considered in this work revealed that increasing nanoparticle concentrations may not necessarily be the most optimal route to improve efficiency. For instance, using ANNs, we determined that the removal of Cu^{2+} was more sensitive to the treatment time and the initial P concentration than the nanoparticle dose. Therefore, a cost-effective approach to increasing treatment

https://doi.org/10.1021/acsestwater.4c00441
ACS EST Water 2024, 4, 3099−3109

efficiency will consider the cost of increasing treatment time, P concentration, and nanoparticle dose before determining the best option for performance enhancement.

■ ASSOCIATED CONTENT

Supporting Information

The Supporting Information is available free of charge at https://pubs.acs.org/doi/10.1021/acsestwater.4c00441.

Additional experimental details; materials and methods; results; dissolved Fe concentration in the supernatant of NZVI suspension after centrifugation; XRD diffractograms of (a) NZVI and (b) $SNZVI_{0.28}$ after treatment; summary of parameters obtained from the adsorption kinetics models, and summary of parameters obtained from the adsorption isotherm models (PDF)

■ AUTHOR INFORMATION

Corresponding Author

Adeyemi S. Adeleye − *Department of Civil and Environmental Engineering, University of California, Irvine, Irvine, California 92697-2175, United States; Department of Earth and Environmental Engineering, Columbia University, New York, New York 10027-6623, United States;* orcid.org/0000-0002-2181-4922; Phone: (212) 854-8989; Email: asa2296@columbia.edu

Author

Ziwei Han − *Department of Civil and Environmental Engineering, University of California, Irvine, Irvine, California 92697-2175, United States*

Complete contact information is available at: https://pubs.acs.org/10.1021/acsestwater.4c00441

Author Contributions

CRediT: **Ziwei Han** conceptualization, data curation, formal analysis, investigation, methodology, writing-original draft, writing-review & editing; **Adeyemi S. Adeleye** conceptualization, data curation, formal analysis, funding acquisition, investigation, project administration, resources, supervision, visualization, writing-original draft, writing-review & editing.

Notes

The authors declare no competing financial interest.

■ ACKNOWLEDGMENTS

The SEM, TEM, BET, XRD, and XPS analyses were performed at the UC Irvine Materials Research Institute (IMRI). IMRI is supported in part by the National Science Foundation through the UC Irvine Materials Research Science and Engineering Center (DMR-2011967). The authors acknowledge the Laser Spectroscopy Laboratories (LSL) at UC Irvine for access to their Raman spectroscopy equipment.

■ REFERENCES

(1) Sharma, S.; Nagpal, A. K.; Kaur, I. Heavy metal contamination in soil, food crops and associated health risks for residents of Ropar wetland, Punjab, India and its environs. *Food Chem.* **2018**, *255*, 15−22.

(2) Barber, R. G.; Grenier, Z. A.; Burkhead, J. L. Copper toxicity is not just oxidative damage: Zinc systems and insight from Wilson disease. *Biomedicines* **2021**, *9* (3), No. 316.

(3) Sun, Z.; Xie, X.; Wang, P.; Hu, Y.; Cheng, H. Heavy metal pollution caused by small-scale metal ore mining activities: A case study from a polymetallic mine in South China. *Sci. Total Environ.* **2018**, *639*, 217−227.

(4) Saha, N.; Rahman, M. S.; Ahmed, M. B.; Zhou, J. L.; Ngo, H. H.; Guo, W. Industrial metal pollution in water and probabilistic assessment of human health risk. *J. Environ. Manage.* **2017**, *185*, 70−78.

(5) Lu, H.; Yu, S. Spatio-temporal variational characteristics analysis of heavy metals pollution in water of the typical northern rivers, China. *J. Hydrol.* **2018**, *559*, 787−793.

(6) Liu, W.-R.; Zeng, D.; She, L.; Su, W.-X.; He, D.-C.; Wu, G.-Y.; Ma, X.-R.; Jiang, S.; Jiang, C.-H.; Ying, G.-G. Comparisons of pollution characteristics, emission situations, and mass loads for heavy metals in the manures of different livestock and poultry in China. *Sci. Total Environ.* **2020**, *734*, No. 139023.

(7) Qi, Y.; Zhao, Y.; Fu, G.; Li, J.; Zhao, C.; Guan, X.; Zhu, S. The Nutrient and Heavy Metal Contents in Water of Tidal Creek of the Yellow River Delta, China: Spatial Variations, Pollution Statuses, and Ecological Risks. *Water* **2022**, *14* (5), No. 713, DOI: 10.3390/w14050713.

(8) Vardhan, K. H.; Kumar, P. S.; Panda, R. C. A review on heavy metal pollution, toxicity and remedial measures: Current trends and future perspectives. *J. Mol. Liq.* **2019**, *290*, No. 111197.

(9) Carolin, C. F.; Kumar, P. S.; Saravanan, A.; Joshiba, G. J.; Naushad, M. Efficient techniques for the removal of toxic heavy metals from aquatic environment: A review. *J. Environ. Chem. Eng.* **2017**, *5* (3), 2782−2799.

(10) Faur-Brasquet, C.; Kadirvelu, K.; Le Cloirec, P. Removal of metal ions from aqueous solution by adsorption onto activated carbon cloths: adsorption competition with organic matter. *Carbon* **2002**, *40* (13), 2387−2392.

(11) Campos, N. F.; Guedes, G. A.; Oliveira, L. P.; Gama, B. M.; Sales, D. C.; Rodriguez-Diaz, J. M.; Barbosa, C. M.; Duarte, M. M. Competitive adsorption between Cu2+ and Ni2+ on corn cob activated carbon and the difference of thermal effects on mono and bicomponent systems. *J. Environ. Chem. Eng.* **2020**, *8* (5), No. 104232.

(12) Faraji, S.; Rahim, A. A.; Mohamed, N.; Sipaut, C. S. Electroless copper-phosphorus coatings with the addition of silicon carbide (SiC) particles. *Int. J. Miner., Metall. Mater.* **2011**, *18*, 615−622.

(13) Peligro, F. R.; Pavlovic, I.; Rojas, R.; Barriga, C. Removal of heavy metals from simulated wastewater by in situ formation of layered double hydroxides. *Chem. Eng. J.* **2016**, *306*, 1035−1040.

(14) Haynes, W. M. *CRC Handbook of Chemistry and Physics*; CRC Press, 2016.

(15) Myers, R. J. The new low value for the second dissociation constant for H2S: its history, its best value, and its impact on the teaching of sulfide equilibria. *J. Chem. Educ.* **1986**, *63* (8), No. 687.

(16) Basha, C. A.; Bhadrinarayana, N.; Anantharaman, N.; Begum, K. M. S. Heavy metal removal from copper smelting effluent using electrochemical cylindrical flow reactor. *J. Hazard. Mater.* **2008**, *152* (1), 71−78.

(17) Mohan, D.; Sarswat, A.; Ok, Y. S.; Pittman, C. U., Jr Organic and inorganic contaminants removal from water with biochar, a renewable, low cost and sustainable adsorbent−a critical review. *Bioresour. Technol.* **2014**, *160*, 191−202.

(18) Eljamal, O.; Mokete, R.; Matsunaga, N.; Sugihara, Y. Chemical pathways of nanoscale zero-valent iron (NZVI) during its transformation in aqueous solutions. *J. Environ. Chem. Eng.* **2018**, *6* (5), 6207−6220.

(19) Tang, H.; Wang, J.; Zhang, S.; Pang, H.; Wang, X.; Chen, Z.; Li, M.; Song, G.; Qiu, M.; Yu, S. Recent advances in nanoscale zero-valent iron-based materials: Characteristics, environmental remediation and challenges. *J. Cleaner Prod.* **2021**, *319*, No. 128641.

(20) Adeleye, A. S.; Conway, J. R.; Garner, K.; Huang, Y.; Su, Y.; Keller, A. A. Engineered nanomaterials for water treatment and remediation: Costs, benefits, and applicability. *Chem. Eng. J.* **2016**, *286*, 640−662.

(21) Han, Z.; Adeleye, A. S.; Keller, A. A. Engineered Nanomaterials for Water Treatment. In *Reference Module in Materials Science and Materials Engineering*; Elsevier, 2021.

(22) Govedarica, J. J.; Tomašević Pilipović, D.; Gvoić, V.; Kerkez, Đ.; Maćerak, A. L.; Slijepčević, N.; Bečelić-Tomin, M. Eco-friendly nanoparticles: mechanisms and capacities for efficient removal of heavy metals and phosphate from water using definitive screening design approach. *Environ. Geochem. Health* **2024**, *46* (4), No. 118.
(23) Han, Z.; Salawu, O. A.; Zenobio, J. E.; Zhao, Y.; Adeleye, A. S. Emerging investigator series: immobilization of arsenic in soil by nanoscale zerovalent iron: role of sulfidation and application of machine learning. *Environ. Sci.: Nano* **2021**, *8* (3), 619−633.
(24) Su, Y.; Jassby, D.; Zhang, Y.; Keller, A. A.; Adeleye, A. S. Comparison of the colloidal stability, mobility, and performance of nanoscale zerovalent iron and sulfidated derivatives. *J. Hazard. Mater.* **2020**, *396*, No. 122691.
(25) Su, Y.; Adeleye, A. S.; Huang, Y.; Zhou, X.; Keller, A. A.; Zhang, Y. Direct Synthesis of Novel and Reactive Sulfide-modified Nano Iron through Nanoparticle Seeding for Improved Cadmium-Contaminated Water Treatment. *Sci. Rep.* **2016**, *6*, No. 24358.
(26) Su, Y.; Adeleye, A. S.; Keller, A. A.; Huang, Y.; Dai, C.; Zhou, X.; Zhang, Y. Magnetic sulfide-modified nanoscale zerovalent iron (S-nZVI) for dissolved metal ion removal. *Water Res.* **2015**, *74* (0), 47−57.
(27) Arshadi, M.; Abdolmaleki, M.; Eskandarloo, H.; Azizi, M.; Abbaspourrad, A. Synthesis of highly monodispersed, stable, and spherical NZVI of 20−30 nm on filter paper for the removal of phosphate from wastewater: batch and column study. *ACS Sustainable Chem. Eng.* **2018**, *6* (9), 11662−11676.
(28) Adeleye, A. S.; Ho, K. T.; Zhang, M.; Li, Y.; Burgess, R. M. Fate and transformation of graphene oxide in estuarine and marine waters. *Environ. Sci. Technol.* **2019**, *53* (10), 5858−5867.
(29) Salawu, O. A.; Olivares, C. I.; Adeleye, A. S. Adsorption of PFAS onto secondary microplastics: A mechanistic study. *J. Hazard. Mater.* **2024**, *470*, No. 134185.
(30) Rugnini, L.; Costa, G.; Congestri, R.; Antonaroli, S.; Di Toppi, L. S.; Bruno, L. Phosphorus and metal removal combined with lipid production by the green microalga Desmodesmus sp.: An integrated approach. *Plant Physiol. Biochem.* **2018**, *125*, 45−51.
(31) *Method 365.3: Phosphorous, All Forms (Colorimetric, Ascorbic Acid, Two Reagent)*; USEPA: Washington (DC), 1978.
(32) Kerber, S.; Barr, T.; Mann, G.; Brantley, W.; Papazoglou, E.; Mitchell, J. The complementary nature of X-ray photoelectron spectroscopy and angle-resolved X-ray diffraction part I: background and theory. *J. Mater. Eng. Perform.* **1998**, *7*, 329−333.
(33) Eljamal, O.; Khalil, A. M.; Sugihara, Y.; Matsunaga, N. Phosphorus removal from aqueous solution by nanoscale zero valent iron in the presence of copper chloride. *Chem. Eng. J.* **2016**, *293*, 225−231.
(34) Ayob, A.; Ismail, N.; Teng, T. T.; Abdullah, A. Z. Immobilization of Cu2+ using stabilized nano zero valent iron particles in contaminated aqueous solutions. *Environ. Prot. Eng.* **2012**, *38* (3), 119−131.
(35) Liang, L.; Li, X.; Guo, Y.; Lin, Z.; Su, X.; Liu, B. The removal of heavy metal cations by sulfidated nanoscale zero-valent iron (S-nZVI): The reaction mechanisms and the role of sulfur. *J. Hazard. Mater.* **2021**, *404*, No. 124057.
(36) Almeelbi, T.; Bezbaruah, A. Aqueous Phosphate Removal Using Nanoscale Zero-Valent Iron. In *Nanotechnology for Sustainable Development*; Springer 2014; pp 197−210.
(37) Bhattacharjee, S.; Darwish, N.; Shanableh, A. Phosphate removal using nanoscale zerovalent iron: Impact of chitosan and humic acid. *J. Environ. Chem. Eng.* **2020**, *8* (5), No. 104131.
(38) AKSU, G.; Güzeller, C. O.; Eser, M. T. The effect of the normalization method used in different sample sizes on the success of artificial neural network model. *Int. J. Assess. Tools Educ.* **2019**, *6* (2), 170−192.
(39) Cao, M.; Alkayem, N. F.; Pan, L.; Novák, D.; Rosa, J. *Advanced Methods in Neural Networks-Based Sensitivity Analysis with Their Applications in Civil Engineering*; INTECH Press, 2016.
(40) Martínez-Sierra, J. G.; Blas, O. G. S.; Gayón, J. M. M.; Alonso, J. I. G. Sulfur analysis by inductively coupled plasma-mass spectrometry: A review. *Spectrochim. Acta, Part B* **2015**, *108*, 35−52.
(41) Adeleye, A. S.; Keller, A. A.; Miller, R. J.; Lenihan, H. S. Persistence of commercial nanoscaled zero-valent iron (nZVI) and by-products. *J. Nanopart. Res.* **2013**, *15* (1), No. 1418.
(42) Stevenson, L. M.; Adeleye, A. S.; Su, Y.; Zhang, Y.; Keller, A. A.; Nisbet, R. M. Remediation of Cadmium Toxicity by Sulfidized Nano-Iron: The Importance of Organic Material. *ACS Nano* **2017**, *11* (10), 10558−10567.
(43) Xu, J.; Avellan, A.; Li, H.; Liu, X.; Noël, V.; Lou, Z.; Wang, Y.; Kaegi, R.; Henkelman, G.; Lowry, G. V. Sulfur loading and speciation control the hydrophobicity, electron transfer, reactivity, and selectivity of sulfidized nanoscale zerovalent iron. *Adv. Mater.* **2020**, *32* (17), No. 1906910.
(44) Su, Y.; Adeleye, A. S.; Keller, A. A.; Huang, Y.; Dai, C.; Zhou, X.; Zhang, Y. Magnetic sulfide-modified nanoscale zerovalent iron (S-nZVI) for dissolved metal ion removal. *Water Res.* **2015**, *74*, 47−57.
(45) Li, Y.; Yue, Q.; Gao, B. Adsorption kinetics and desorption of Cu (II) and Zn (II) from aqueous solution onto humic acid. *J. Hazard. Mater.* **2010**, *178* (1−3), 455−461.
(46) Christ, B. V. Handbook of Monochromatic XPS Spectra. In *Elements and Native Oxides*; XPS International, 2000.
(47) Ge, J.; Ding, X.; Jiang, D.; Zhang, L.; Du, P. Efficient improved charge separation of FeP decorated worm-like nanoporous BiVO 4 photoanodes for solar-driven water splitting. *Catal. Lett.* **2021**, *151*, 1231−1238.
(48) Ge, X.; Wang, L.; Zhang, W.; Putnis, C. V. Molecular understanding of humic acid-limited phosphate precipitation and transformation. *Environ. Sci. Technol.* **2020**, *54* (1), 207−215.
(49) Adeleye, A. S.; Stevenson, L. M.; Su, Y.; Nisbet, R. M.; Zhang, Y.; Keller, A. A. Influence of phytoplankton on fate and effects of modified zerovalent iron nanoparticles. *Environ. Sci. Technol.* **2016**, *50* (11), 5597−5605.
(50) Bădică, C. E.; Chiriță, P. An electrochemical study of the oxidative dissolution of iron monosulfide (FeS) in air-equilibrated solutions. *Electrochim. Acta* **2015**, *178*, 786−796.

https://doi.org/10.1021/acsestwater.4c00441
ACS EST Water 2024, 4, 3099−3109